Arch. Metall. Mater. **71** (2026), 1, 157-172

DOI: https://doi.org/10.24425/amm.2026.157778

H. KERBICHE[1], A. CHADLI[2,3*], A. CHERIET[4]

PRESSURE EFFECTS ON THE STRUCTURAL, MECHANICAL AND OPTO-ELECTRONIC PROPERTIES OF POTASSIUM-BASED ANTIPEROVSKITES K_3XO (X = Cl, Br, I) FROM FIRST-PRINCIPLES INVESTIGATION

Herein, using first-principle calculations and full potential linearized augmented plane wave, the structural, mechanical, and opto-electronic properties of K_3XO (X = Cl, Br, and I) anti-perovskite oxides have been studied under different pressures. The structures optimization shows cell parameters very close to the available experimental and theoretical values. The mechanical stability criteria is checked by computed the elastic constants C_{11}, C_{12} and C_{44} using the optimized data. Our results also demonstrate the ductility of the all compounds under study and their usefulness in medium-temperature devices, as they have a relatively high Debye temperature. Furthermore, the calculated band structure revealed a direct band gap for the three antiperovskites, the energy band gap values are about 4.21, 3.55 and 3.16 eV for K_3ClO, K_3BrO and K_3IO, respectively, these values of E_g increase linearly as a function of pressure. We investigate also the optical properties of these compounds under various pressures, such as the dielectric function, absorption coefficient, energy loss function, reflectivity and refractive index, within the photon energy interval 0-25 eV, hence all the studied antiperovskites exhibit excellent optical properties, including low reflectivity and high absorption in the ultraviolet region which is good for photovoltaic applications.

Keywords: First-principle calculations; Antiperovskites; Electronic band structure; Optical properties; Elastic constants

1. Introduction

Following the discovery and interesting technological applications of ABO_3 perovskite-type compounds [1-3], with the ideal cubic structure (space group $Pm\bar{3}m$), which have many physical and chemical phenomena such as multiferroicity, ferroelectricity, magnetism, superconductivity and catalysts [1]. They have been also used in various technologies such as magnetic random-access memories, colossal magnetoresistance (CMR), photocatalytic, photovoltaic, magnetocaloric, magnetic refrigeration technology (MR), gas sensor, electrical field sensors, and as protector of electric shocks in electronic devices [4-11]. In recent years, for scientific challenges and technological requirements, research associated with the perovskites has been considerably triggered towards other similar structures, such as hybrid perovskites [12] and antiperovskites or inverse perovskites [13]. The antiperovskites (APV) compounds of formula A_3BX have an identical perovskites structure but with cations replaced by anions and vice versa. In addition, based on the chemical composition of antiperovskites compounds, they can have different behaviours such as metallicity, semi-conductivity or superconductivity [15-17]. They are also technologically important due to their numerous interesting properties, including giant magnetoresistance and giant magnetostriction in Mn_3CuN [18,19] spin glass behaviour in $GeNCo_3$ [20], and unique physical properties namely almost zero temperature resistance coefficient, negative thermal expansion, and high ionic conductivities in Cr_3LiN and Na_3OCl [21-22]. Moreover, low bandgap antiperovskites have been considered as promising candidates for applications in optical devices in K_3BrO [23] and for the development of new electrochemical energy storage devices and clean energy resources in Li_3OX (X = Cl, Br, I) [24,25]. Elsewhere, other semiconductor antiperovskite compounds are more attractive because of their thermoelectric behaviour, such behaviours were observed in K_3ISe, K_3ITe and Rb_3AuO [26-27]. Other recent studies have also shown that certain nitride-based inverse perovskites are potential candidates for topological crystalline insulators and massless 3D Dirac systems [28-29]. Among the antiperovskite compounds studied are those mainly constructed from alkali elements of formula A_3OX (or A_3XO) in which A denotes the cation (Li, Na, or K) and X represents halogen atom (Cl, Br, or I). These inorganic compounds are lightweight and electrochemically

[1] MOHAMED KHIDER UNIVERSITY OF BISKRA, LCME LABORATORY, 07000, BISKRA, ALGERIA
[2] MOHAMED KHIDER UNIVERSITY OF BISKRA, LARHYSS LABORATORY, 07000, BISKRA, ALGERIA
[3] MOHAMED KHIDER UNIVERSITY OF BISKRA, LIMIA LABORATORY, 07000, BISKRA, ALGERIA.
[4] AMAR TELIDJI UNIVERSITY OF LAGHOUAT, LPCM LABORATORY, 03000 LAGHOUAT, ALGERIA

* Corresponding author: hakim.chadli@univ-biskra.dz

stable and possess promising ionic conductivity. Hence, researchers have focused sodium and potassium-based antiperovskites, because their great abundance reduces the manufacturing cost of the various devices. Sabrowsky, Hipper et al. in 1988 then in 1990 were the first who discussed the existence of ternary alkali metal chalcogenide halides and their crystal structure, which are sodium-based antiperovskites Na_3OCl and Na_3OBr [30,31]. These materials adopt a cubic structure with space group $Pm\bar{3}m$ (N° 221), while the lattice parameter a is found to be 4.50 and 4.57 Å, respectively [30,31]. One years later (1991), Sitta et al. conducted two studies on the crystal structure of the antiperovskites K_3OBr, and K_3IO, where they reported that these oxides crystallize also in cubic system with lattice parameter is about 5.21 and 5.28 Å respectively [32,33].

Meanwhile, several theoretical studies were also focused on this type of compounds [15,34-37]. First, Zinenko et al. conducted a theoretical study targeting the lattice dynamics of antiperovskite structure compounds A_3OX (A = Na, K; X = CI, Br) [34]. Whereas, Ramanna et al. studied the electronic structure, elastic and optical properties of Na_3OCl, Na_3OBr, and K_3OBr antiperovkites [35]. Furthermore, Long et al. and Khandy et al. were studied the electronic, elastic, and dynamic properties of Na_3OBr and electronic, thermomechanical and phonon properties of Na_3OCl, respectively [15,36]. Moreover, Sattar et al. were published a short communication about all the antiperovskites oxides of formula A_3OX (A = Li, Na and K; X = CI, Br and I), targeting the structural stability, lattice dynamics, electronic, thermophysical, and mechanical properties [37]. However, based on the available informations and to the best of our knowledge, there are scarce studies on potassium-based antiperovskites, its properties and its applications. Hence, the optical properties of K_3XO antiperovskites (X = CI, Br and I), have never been a subject of research. In addition, there is no contribution (either theoretically or experimentally) about the pressure effect on different properties of calcium-based antiperovskites. For these reasons, our main objective in this work is to predict the effect pressure on different properties of K_3XO (X = Cl, Br and I) antiperovskites, such as, mechanical stabilities, elastic, electronic and optical properties. We present a series of first-principles calculations using the density functional theory (DFT) and full-potential linearized augmented plane wave (FP-LAPW). The paper's succeeding parts are organized as follows; after this introduction, the methodology used in this research is briefly discussed in Section 2. In Section 3, we describe and analyse our results, and in the conclusion, we provide a brief overview about what we found.

2. Calculation methodology

The present study employed density functional theory (DFT) [38] based on Kohn-Sham equations [39] and full potential linearized augmented plane wave (FP-LAPW) method [40] as implemented in the WIEN2k package [41], to examine the structural, mechanical, electronic, and optical properties of A_3XO anti-perovskites (X = Cl, Br and I). The evaluation of the exchange-correlation potential was conducted the generalized gradient approximation, as described by Wu and Cohen (WC-GGA) [42]. The Tran-Blaha modified Becke-Johnson TB-mBJ approach was also employed to calculate the electronic and optical properties with the highest level of accuracy [43]. In the FP-LAPW method, the compound's unit cell is partitioned into two distinct parts: the interstitial region (IR) and the muffin-tin spherical region (MT). The R_{MT} was chosen to be 1.8, 1.5, 1.8, 1.9 and 2.0 (au) for K, O, Cl, Br and I atoms, respectively, while, the $R_{MT} \times K_{\max}$ parameter was set to be 8, where R_{MT} is the smallest muffin-tin radius and $K_{\max}$ is the maximum plane wave vector in the *k*-space. A Monkhorst-Pack k-mesh [44] as $15 \times 5 \times 15$ (which gives 120 Kpts) was used for the integration in the Brillouin zone. The self-consistent integrations are considered to be converged when the energy is stable within 10^{-6}Ryd.

3. Result and discussion

In this section, we provides a comprehensive analysis of the results of our calculations on the different properties of K_3XO anti-perovskite oxides (X = Cl, Br and I). Targeting the mechanical stability, and pressure effect on elastic, electronic and optical properties.

3.1. Structural properties and optimization

First, the geometries of K_3XO antiperovskites were fully optimized using the available experimental and theoretical data [32-37]. Therefore, we calculate the total system energy at different volumes. In the space group $Pm\bar{3}m$ (N° 221), the K_3XO compounds have one formula per unit cell, with atoms occupying specific Wyckoff locations. Where, the metal cations (A) are located in the center of faces (0, 0.5, 0.5) instead of oxygen anions (in perovskite structure) which are displaced towards the cube center (0.5, 0.5, 0.5), and the eight vertexes are occupied by X anion in the position (0, 0, 0) [15,34]. We note that the only available experimental lattice parameters are those observed for K_3BrO and K3IO antiperovskites about 5.21 and 5.28 Å, respectively [32,33]. Once the total energy is determined at various volumes, the geometry is determined by fitting the energy-volume data using the Birch-Murnaghan equation of state [45] (see Fig. 1):

$$E(V) = E_0 + \frac{9V_0B}{16}\left\{\left[\left(\frac{V_0}{V}\right)^{\frac{2}{3}} - 1\right]^3 B' + \left[\left(\frac{V_0}{V}\right)^{\frac{2}{3}} - 1\right]^2\left[6 - 4\left(\frac{V_0}{V}\right)^{\frac{2}{3}}\right]\right\} \quad (1)$$

Where, $E(V)$ represents the total energy at the deformed volume (V), E_0 the total energy at reference (V_0) volume, B the bulk

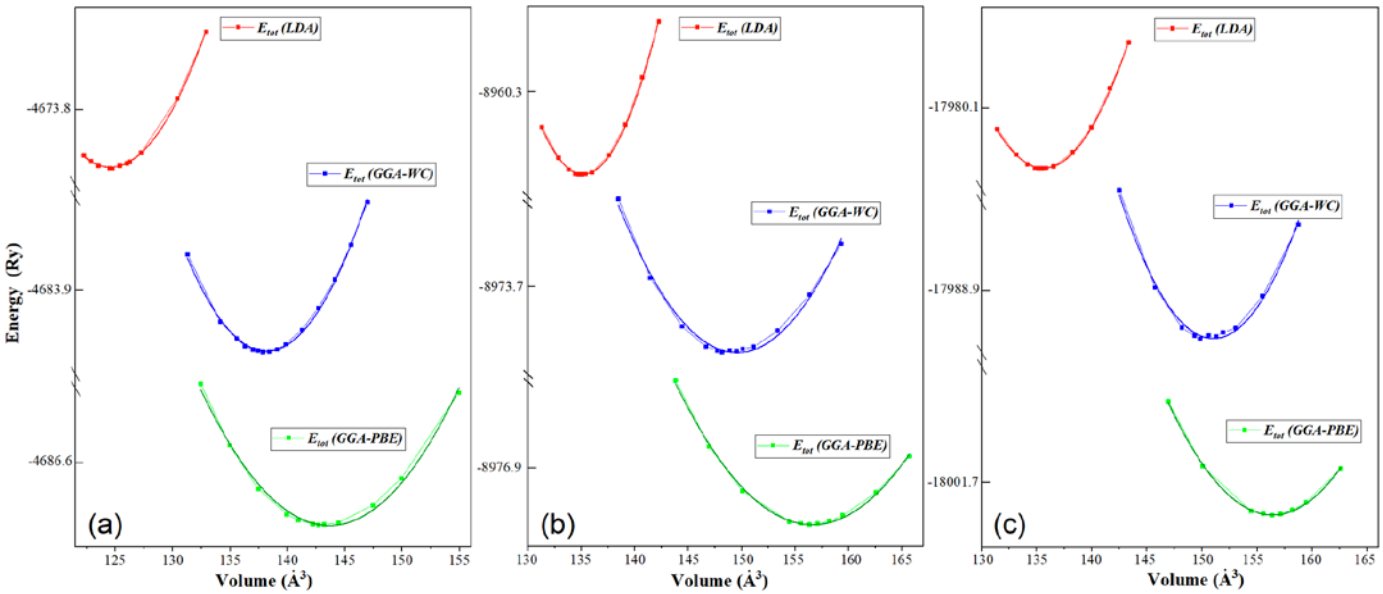

Fig. 1. The E-V curve estimated based on the Birch-Murnaghan equation of state of (a) K_3ClO, (b) K_3BrO and (c) K_3IO at 0 GPa using LDA, GGA-WC and GGA-PBE approximations

TABLE 1

The optimized and under pressure calculated lattice constant a_0, volume V at equilibrium, bulk modulus B and its pressure derivate B' of K_3XO (X = Cl, Br and I) antiperovskites

Compound	Method	P (GPa)	a_0 (Å)		V (Å^3)	B (GPa)	B'
			This work	Other work			
K_3ClO	LDA	0	4.996	4.76 [34] 5.22 [37]	124.745	27.063	4.615
	GGA-PBE	0	5.225		142.687	19.360	4.492
	GGA-WC	**0**	5.141		135.906	20.83	3.882
		5	4.858		114.646	—	—
		10	4.696		103.593	—	—
		15	4.584		96.348	—	—
		20	4.498		91.047	—	—
K_3BrO	LDA	0	5.041	exp. 5.21 [32] 4.81 [34] 5.28 [35] 5.28 [37]	128.168	26.994	5.321
	GGA-PPE	0	5.282		147.390	18.997	4.794
	GGA-WC	**0**	5,182		139.176	20.478	4.560
		5	4.910		118.384	—	—
		10	4.760		107.893	—	—
		15	4.658		101.103	—	—
		20	4.581		96.165	—	—
K_3IO	LDA	0	5.130	exp. 5.28 [33] 5.38 [37]	135.066	26.411	5.252
	GGA-PBE	0	5.387		156.338	18.217	3.994
	GGA-WC	**0**	5.279		147.147	19.850	4.727
		5	4.994		124.591	—	—
		10	4.844		113.660	—	—
		15	4.742		106.633	—	—
		20	4.665		101.538	—	—

modulus and B' denotes bulk modulus derivate with respect to pressure.

The equilibrium volume is that corresponds to the minimum energy. The results of the DFT-FP-LAPW calculations at different pressure (from 0 to 20 GPa) and experimental data of lattice parameters, Bulk modulus B and its pressure derivation B' are summarized in TABLE 1, and the variation of volume against pressure is plotted in Fig. 2. From TABLE 1, we can clearly see that the lattice parameter (at 0 GPa) grows significant as X element goes in order of increasing the atomic number. This is because the size of the ions increases in the order $Cl^- < Br^- < I^-$. In contrast, the elastic modulus B decreases from K_3IO to K_3ClO, suggesting a reduction in hardness in this way. These results are comparable to the experimental data and other theoretical results available in literature [34,35,37]. We note here that the results obtained using the GGA-WC are more comparable to the experi-

mental data compared to GGA-PBE and LDA approximations, so, we will proceed just the GGA-WC approximation for the rest of our work. Under pressure, the volume (lattice parameter) of all compounds decrease significantly as shown in Fig. 2.

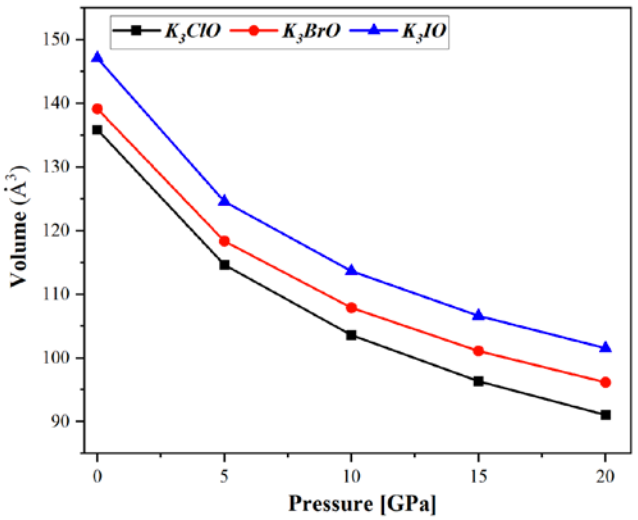

Fig. 2. Optimized volume of K_3XO (X = Cl, Br, I) against pressure

3.3. Mechanical stabilities and pressure dependence of elastic properties

The elastic properties of materials are very important to quantify the deformability of a material when subjected to any stresses and its subsequent ability to revert to its original shape after the stresses are removed. Using the elastic constants that are fundamental to the mechanical and the dynamic properties, we can obtain valuable informations of a material, such as chemical bonding, stability and stiffness, specific heat, thermal expansion, Debye temperature, Grüneisen parameter, melting point and so on. We have used the theoretical model developed by Thomas Charpin and integrated it in the WIEN2k package to calculate the elastic constants (C_{ij}) of K_3ClO, K_3BrO and K_3IO antiperovkites. The cubic system is characterized by three distinct elastic constants, specifically C_{11}, C_{12}, and C_{44}, of these, only the constant C_{44} has a direct physical meaning as a measure of the crystal's resistance to shear in the cube plane along any direction lying in this plane [46]. Since a cubic material will not be mechanically stable unless [47]:

$$B = (C_{11} + 2C_{12})/3 > 0 \qquad (2)$$

$$C_{11} - C_{12} > 0 \quad \text{and} \quad C_{44} > 0 \qquad (3), (4)$$

The physical interpretation of C_{11} pertains to the elasticity along the axis of unit cell, while the transverse expansion resistance C_{12} and shear deformation resistance C_{44} define the elasticity in shape, which is caused by transverse strain on the structure. The calculated values of C_{ij} using GGA-WC approximation and the several theoretical findings that could be obtained such as Cauchy pressure ($C_p = C_{12}$-C_{44}) are displayed in TABLE 2.

TABLE 2

Calculated values of elastic constants (C_{ij}, in GPa) at different pressure for K_3XO (X = Cl, B and I) antiperovskites

Compound		P [GPa]	Elastic constants [GPa]			
			C_{11}	C_{12}	C_{44}	C_p
K_3ClO	Other work	0	31 [34]	6 [34]	7 [34]	–1 [34]
	This work	0	**53.79**	**7.09**	**9.97**	**–2.88**
		4	102.64	13.13	13.70	–0.57
		8	138.12	18.98	15.02	3.96
		10	155.23	22.01	15.77	6.24
		15	167.29	27.37	17.01	10.36
		20	198.51	30.54	18.46	12.08
K_3BrO	Other work	0	42 [35]	8 [35]	11 [35]	–3 [35]
	This work	0	**48.78**	**8.23**	**11.33**	**–3.10**
		4	86.97	13.11	14.18	–1.07
		8	116.78	20.47	15.49	4.98
		10	133.81	24.73	16.04	8.69
		15	164.08	28.85	17.35	11.50
		20	192.34	32.95	19.46	13.49
K_3IO	Other work	0	17.9 [37]	18.8 [37]	10.7 [37]	8.1 [37]
	This work	0	**43.54**	**9.81**	**13.13**	**–3.32**
		4	90.02	18.60	19.92	–1.32
		8	121.26	24.34	22.90	1.44
		10	136.76	27.13	24.12	3.01
		15	163.25	31.77	27.09	4.68
		20	189.49	35.96	30.23	5.73

Firstly, all the calculated elastic constants are positive and satisfying the stability criteria for cubic crystals, suggesting the mechanical stability of all our compounds [48]. Besides, we can clearly observe that the elastic constants increase linearly under applied pressure (see Fig. 3).

Several additional critical elastic parameters include the bulk Modulus (B), shear Modulus (G), Young's Modulus (Y), Pugh ratio (P_g), and the Poisson's ratio (v) can be derived using these three elastic constants, following the Voigt-Reuss-Hill (VRH) methods [49-51]:

$$B = B_V = B_G = (C_{11} + 2C_{12})/3 \qquad (5)$$

$$G_V = (C_{11} - C_{12} + 3C_{44})/5 \qquad (6)$$

$$G_R = \frac{5(C_{11} - C_{12})C_{44}}{[4C_{44} + 3(C_{11} - C_{12})]} \qquad (7)$$

$$G = \frac{G_V + G_R}{2} \qquad (8)$$

$$E = \frac{9BG}{(3B + G)} \quad \text{and} \quad \nu = \frac{3B - E}{6B} \qquad (9), (10)$$

These quantities are calculated and summarised in TABLE 3, and their variation against applied pressure is plotted in Fig. 4 and Fig. 5. We can observe that the bulk modulus B decreases from K_3ClO to K_3IO, while the shear modulus G and Young's modulus Y increase from K_3ClO to K_3IO. The higher

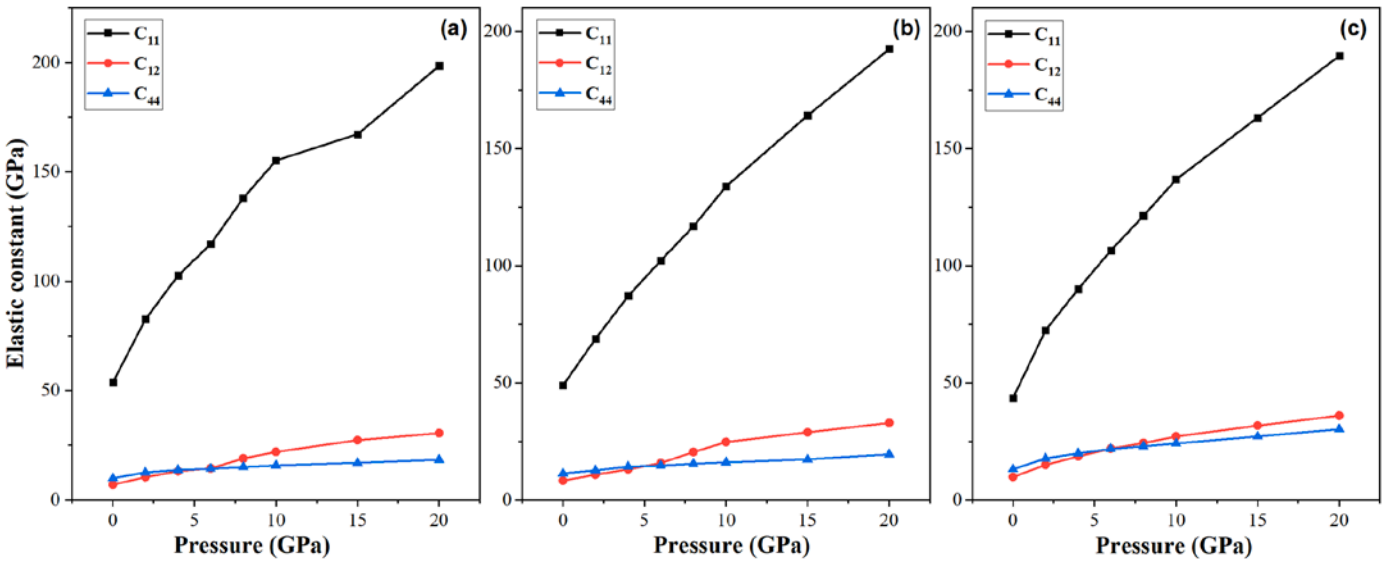

Fig. 3. Calculated elastic constants (C_{ij}) of K_3XO (X = Cl, Br, I) against pressure

values of bulk modulus than shear modulus show the difficulty of the material to change shape rather than length. On the other hand, all materials exhibit a brittle nature (at 0 GPa), since they have a negative value of Cauchy pressure (C_p). This trend is further verified by examining the Pugh ratio ($P_g = B/G$), since $P_g < 1.75$ for all antiperovskites. However, above the pressure of 6 GPa, all materials become ductile in nature. This trend can be confirmed by examining the Poisson's ratio (v), which indicates brittle behavior if $n < 0.333$, which is noted for all our antiperovskites. In addition, Poisson's ratio (v) ca be used to provide information about the type of bond present in a material, its value is indicative of the degree of directionality of the covalent bonds and ranges from –1 to 0.5. This value is small (n = 0.1) for covalent materials, whereas for ionic materials a typical value of n is 0.25 [52]. The calculated Poisson's ratio values are near from 0.25 (0.22, 0.23 and 0.24). Therefore, the ionic contribution to the interatomic bonding for all our materials is dominant. While under applied pressure, the ionic nature of the bonds increases to reach metallic behavior with values of n close to 0.33 [53].

Moreover, to evaluate the elastic anisotropy of crystals, the Zener anisotropy factor A, can be calculated using the following relation [53]:

$$A = \frac{2C_{44}}{(C_{11} - C_{12})} \tag{11}$$

A crystal is anisotropic if its anisotropy factor A value is less than one [54], in this case, all studied compounds are anisotropic since they have A of about for 0.43, 0.56, and 0.78 for K_3ClO for K_3BrO, and K_3IO, respectively. However, under applied pressure the degree of anisotropy increases (see TABLE 3). Currently, there is no experimental data in which we can compare our computational results, so our results are offered as a prediction.

Furthermore, it is more appropriate to describe the elastic anisotropy of Young's modulus with a spherical polar diagram. For this reason, we calculated the elastic compliance constants,

TABLE 3

Calculated bulk modulus (B), shear modulus (G) and Young's modulus (Y) (in GPa) and Pugh's ratio (P_g), Poisson ratio (v) and anisotropic factor (A) (without unity) of Ka_3XO (X = Cl, B and I) antiperovskites

Compound	P [GPa]	B	G	Y	P_g	v	A
K_3ClO	0	**22.66**	**14.13**	**35.09**	**1.60**	**0.24**	**0.43**
	4	42.97	22.54	53.24	1.91	0.28	0.31
	8	58.69	27.14	64.53	2.16	0.30	0.25
	10	66.42	29.40	69.58	2.26	0.31	0.24
	15	73.01	31.29	82.28	2.37	0.31	0.24
	20	86.53	35.75	94.27	2.42	0.32	0.22
K_3BrO	0	**21.78**	**14.35**	**35.29**	**1.52**	**0.23**	**0.56**
	4	37.73	21.05	53.24	1.79	0.26	0.38
	8	52.57	24.01	62.88	2.11	0.30	0.32
	10	61.09	26.91	70.36	2.27	0.31	0.29
	15	73.93	31.07	81.77	2.38	0.32	0.26
	20	86.08	35.72	94.15	2.41	0.32	0.24
K_3IO	0	**21.05**	**14.52**	**35.41**	**1.45**	**0.22**	**0.78**
	4	42.41	25.22	63.14	1.68	0.25	0.56
	8	56.65	31.07	78.81	1.82	0.27	0.47
	10	63.67	33.74	86.03	1.89	0.27	0.44
	15	75.61	38.98	99.80	1.94	0.28	0.41
	20	87.14	44.38	113.81	1.96	0.28	0.39

which are the elements of the inverse matrix of the elastic constants matrix ($S_{ij} = C_{ij}^{-1}$).

The following expression gives dimensional surface for cubic system [55]:

$$\frac{1}{Y} = S_{11} - 2\left(S_{11} - S_{12} - \frac{1}{2}S_{44}\right) \times \left(l_1^2 l_2^2 + l_2^2 l_3^2 + l_3^2 l_1^2\right) \tag{12}$$

Where, l_1, l_2 and l_3 represent the directional cosines with respect to the x, y, and z axes, respectively, and S_{ij} is the elastic compli-

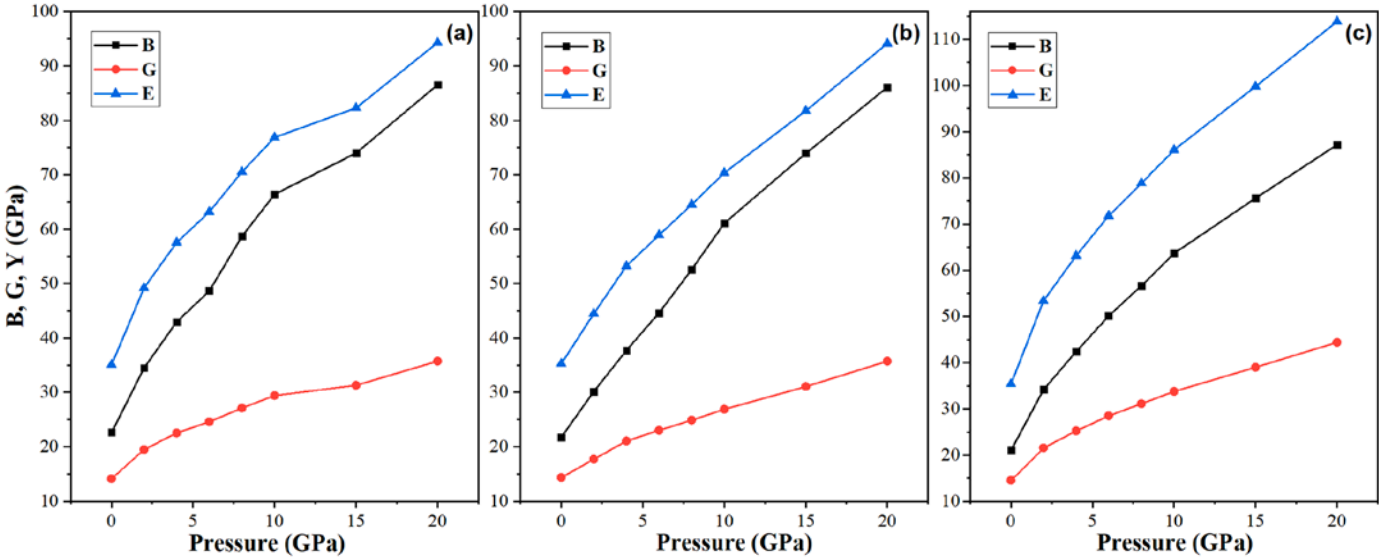

Fig. 4. Calculated elastic moduli (B, G and Y) of K3XO (X = Cl, Br, I) against pressure

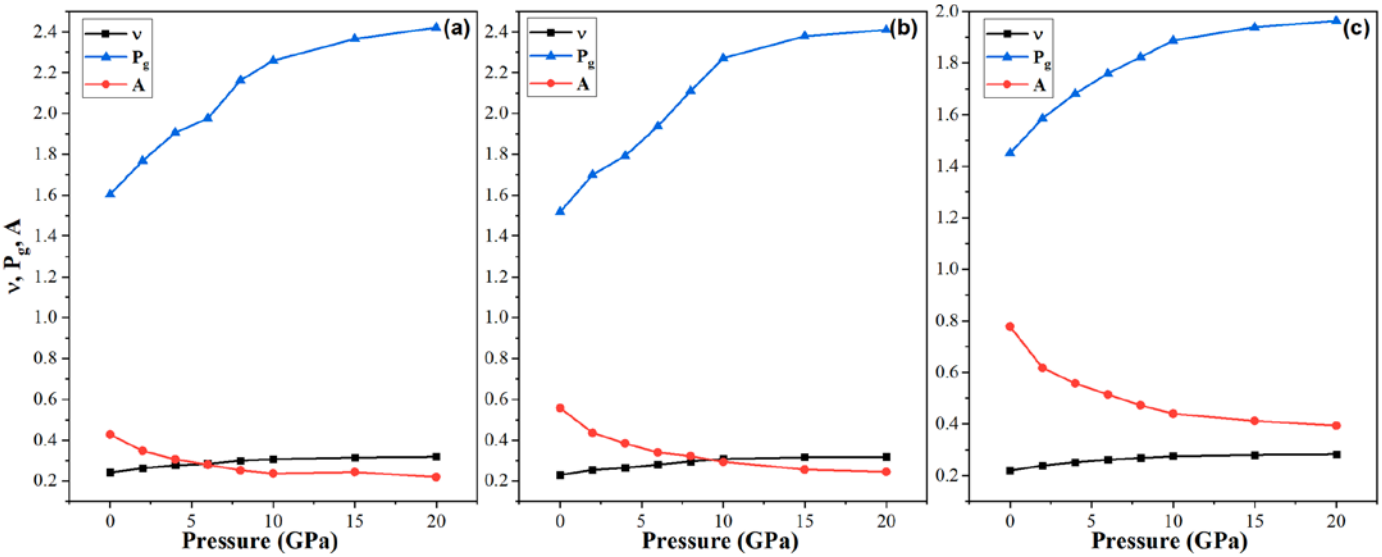

Fig. 5. Calculated Poisson ratio (ν), Pugh's ratio (P_g), and anisotropic factor (A) of K3XO (X = Cl, Br, I) against pressure

ance constant. The 2-dimensional (2D) and 3-dimensional (3D) depictions and the cross-sectional view of Young's modulus for K_3ClO, K_3BrO, and K_3IO are depicted in Figs. 6, 7, and 8, respectively. Based on our analysis, we have concluded that all antiperovskites under study have anisotropic behavior in order $K_3IO < K_3BrO < K_3ClO$ such as was determined by the Zener factor.

The thermal properties such as Debye temperature denoted (θ_D), which is an important parameter in solid-state physics and materials science that characterises the vibrational motion of atoms in a crystal lattice. θ_D is also fundamental parameter that exhibits a close correlation with elastic constants, specific heat, and melting temperature [4]. It is employed to differentiate between regions of elevated and reduced temperatures within a solid. Generally, when the temperature rises above absolute zero, the atoms of the solid gradually vibrate to Debye's temperature. This represents the temperature at which the vibrations reach their maximum of possible modes. It is a good approximation of the hardness of solids. Debye temperature can be determined using the following formula [56]:

$$\theta_D = \frac{h}{k}\left[\frac{3n}{4\pi}\left(\frac{N_A\rho}{M}\right)\right]^{\frac{1}{3}} v_m \qquad (13)$$

TABLE 4

Calculated density ρ (g/cm^3) longitudinal sound velocity v_l (m/s), transverse sound velocity v_t (m/s), average sound velocity v_m (m/s) and Debye temperature θ_D (K) of K_3XO (X = Cl, Br and I) antiperovskites

Compound	ρ	v_l	v_t	v_m	θ_D
K_3ClO	2.08	4466.46	2606.24	2890.68	286.28
K_3BrO	2.53	4049.81	2363.12	2621.03	257.53
K_3IO	2.93	3763.24	2195.89	2435.56	234.91

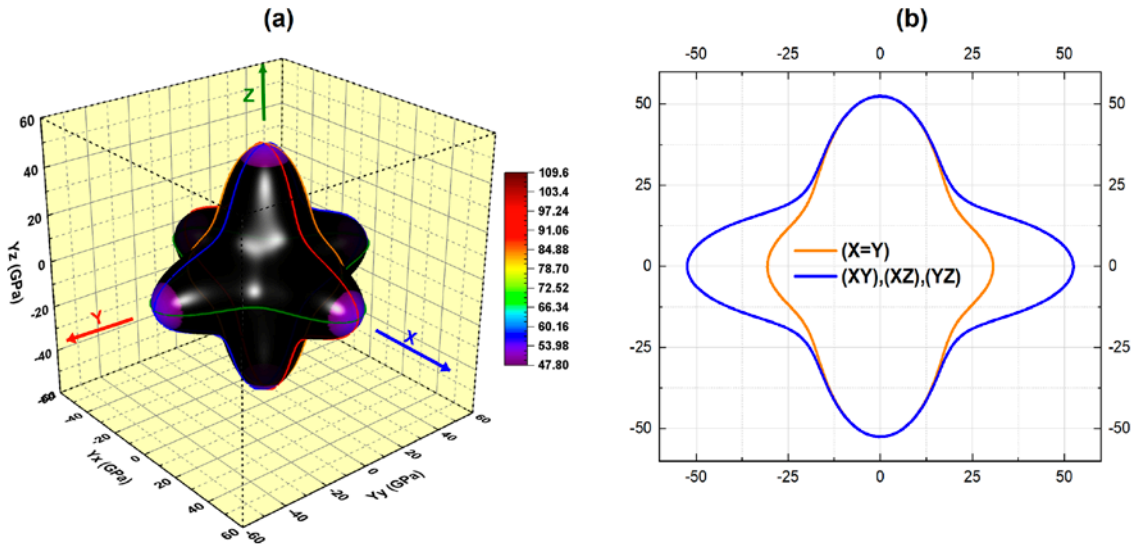

Fig. 6. The 3D-representation (a) and 2D-representation (b) in some reticular planes of Young's modulus for K3ClO antiperovskite

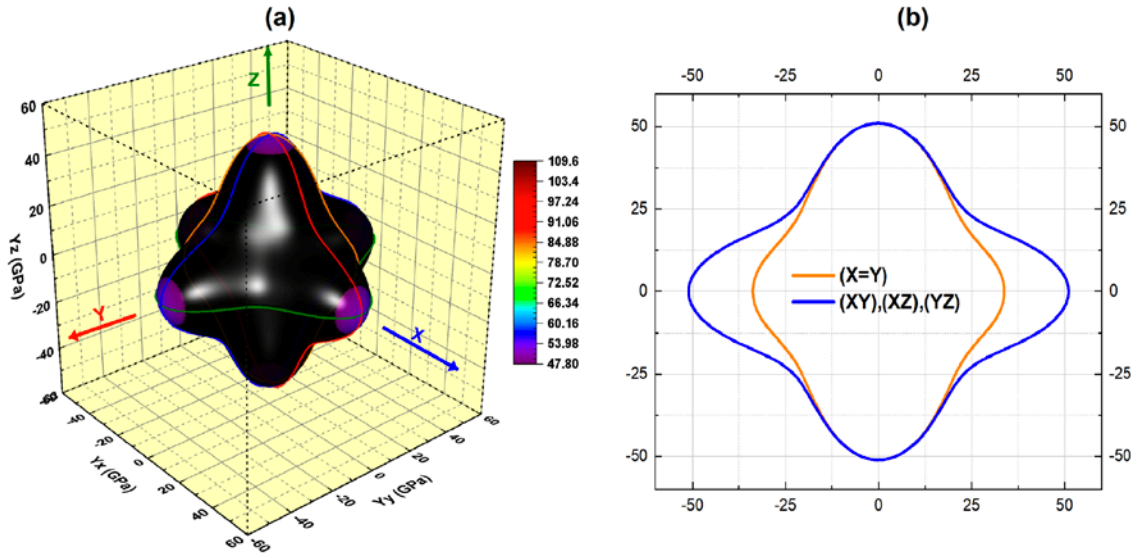

Fig. 7. The 3D-representation (a) and 2D-representation (b) in some reticular planes of Young's modulus for K3BrO antiperovskite

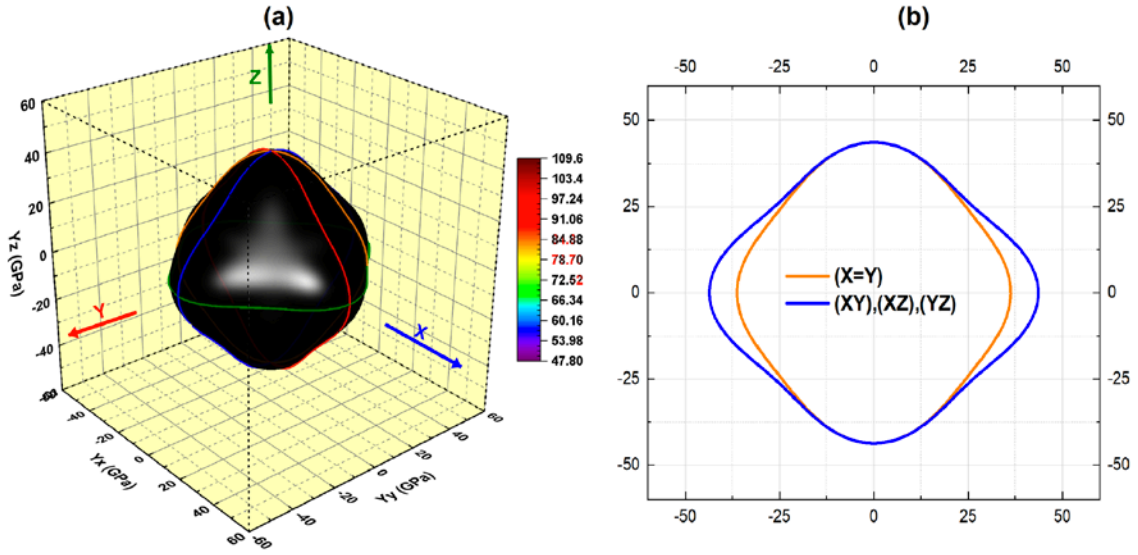

Fig. 8. The 3D-representation (a) and 2D-representation (b) in some reticular planes of Young's modulus for K3IO antiperovskite

In the given context, the symbol h represents the Planck constant, k denotes the Boltzmann constant, n signifies the number of atoms per molecule, ρ represents the density, N_A denotes Avogadro's number, M represents the molecular mass, and v_m represents the average sound velocity which can be given by [57]:

$$v_m = \left[\frac{1}{3}\left(\frac{2}{v_t^3}+\frac{1}{v_l^3}\right)\right]^{-\frac{1}{3}} \quad (14)$$

The variables v_l and v_t represent the longitudinal and transverse sound velocities. The estimation of these two parameters can be derived from the bulk modulus B and the shear modulus G by using Navier's equation in the following manner [57]:

$$v_t = \left(\frac{3B+4G}{3\rho}\right)^{\frac{1}{2}} \text{ and } v_l = \left(\frac{G}{\rho}\right)^{\frac{1}{2}} \quad (15), (16)$$

The values of v_m, v_l, v_t and θ_D calculated using the above formulas are presented in TABLE 4. The calculated Debye's temperature of our compounds is about 286, 257 and 234 K for K_3BrO, K_3ClO, and K_3IO, respectively. We observe that θ_D decreases when the atomic number of X element increase, which means that the iodine-based material is more fragile compared to the other two materials. These values are larger than those obtained in ref [37] about 257, 226 and 202 K for the same materials, whereas, are lower than that found for Na_3OCl about 382 K [31].

3.2. Evaluation of pressurized band structure and electronic state

3.2.1. Band structure

Using GGA-WC approximation [42], then, including TB-mBJ approach [43], we have evaluated the band structure (BS) of cubic antiperovskite compounds K_3XO (X = Cl, Br, I) in the energy range of –8 to 10 eV and at various applied pressures from 0 GPa to 20 GPa. The k-paths used in the band structure analysis are from the irreducible part of the first Brillouin zone. For the cubic system, the k-paths with high symmetry direction used in the band structure are Γ–X–M–Γ–R–X–M–R [58]. The Fermi level (E_F) was defined as the reference energy level with zero energy as shown in Figs. 9, 10 and 11.

The obtained values from DFT-FP-LAPW calculations for the energy band gap of our materials are illustrated in TABLE 5. As shown in Figs. 9, 10 and 11, the semiconducting character of the studied K_3XO materials is confirmed by the absence of energy states at E_F (regardless of the approximation used). Hence, all the studied inverse perovskites exhibit a wide band gap energy above the Fermi level (E_F), where, both the top of valence band (VB) and the bottom of the conduction band (CB) are located at the Γ point for all compounds, consequently a direct band gap was observed for all compounds.

Whereas, the values of E_g using the GGA-WC approximation are about 1.11 eV, 0.98 eV, and 1.13 eV, for K_3ClO, K_3BrO, and K_3IO, respectively. On the other hand, the introducing of TB-mBJ potential gives more significant band gap values

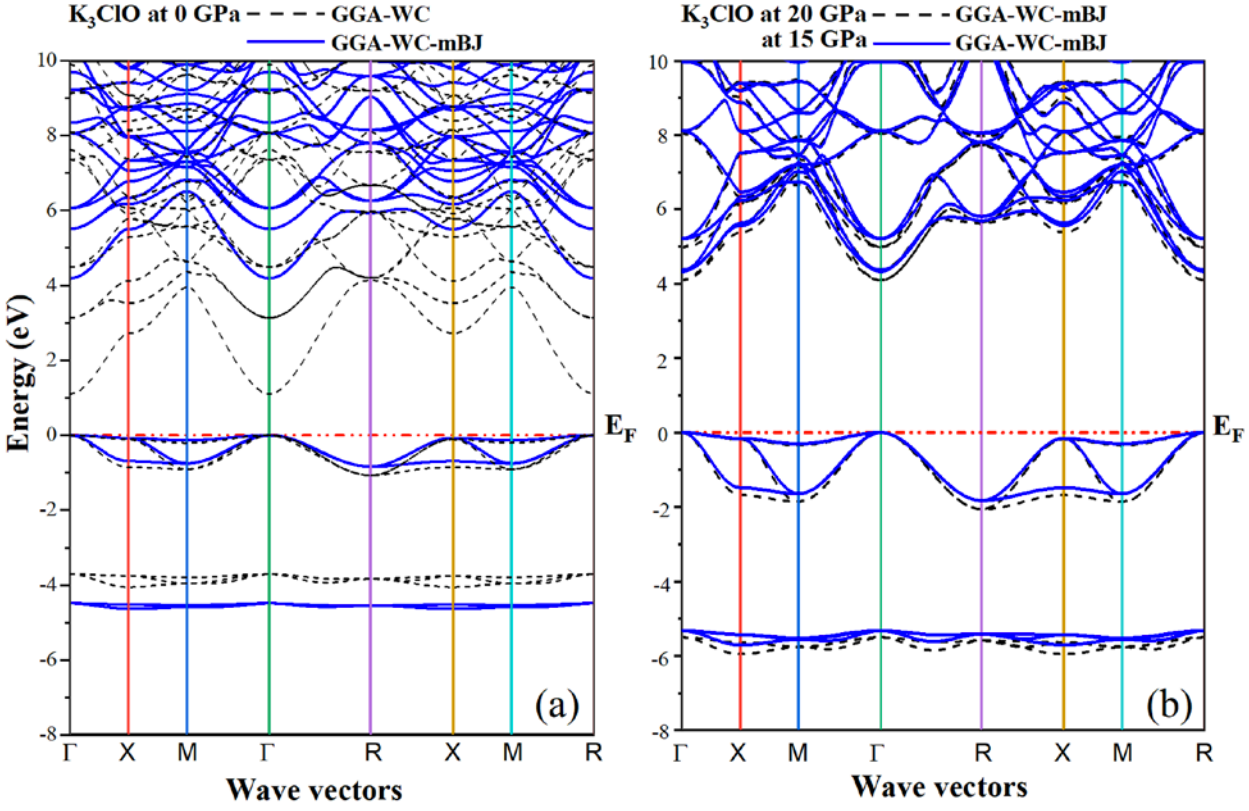

Fig. 9. Electronic band structure of K_3ClO at ambient pressure (0 GPa) and (b) at 15 and 20 GPa

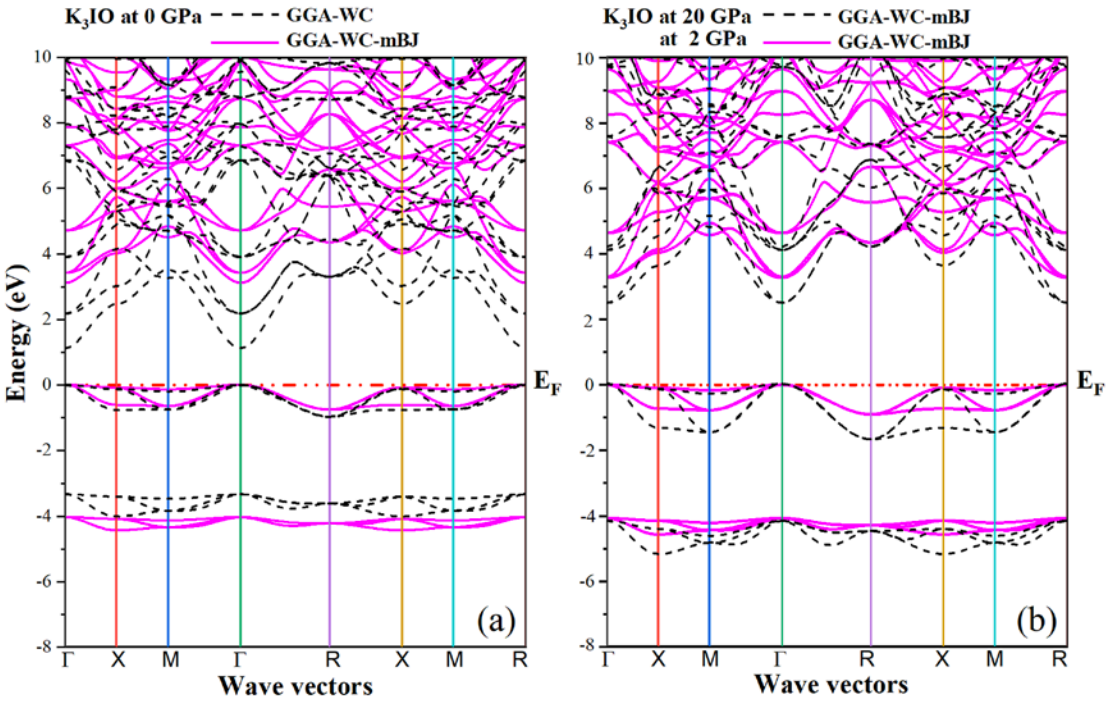

Fig. 10. Electronic band structure of K_3BrO at ambient pressure (0 GPa) and (b) at 12 and 20 GPa

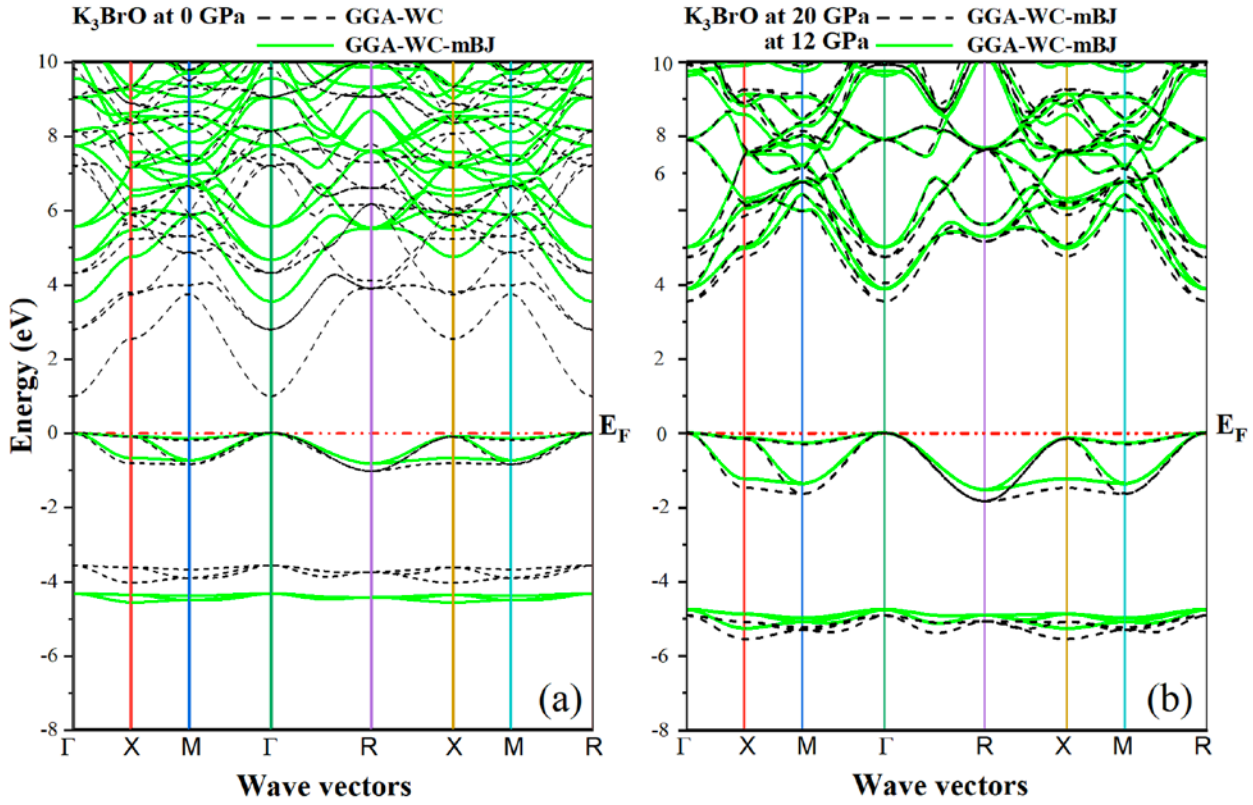

Fig. 11. Electronic band structure of K_3IO at ambient pressure (0 GPa) and (b) at 2 and 20 GPa

to be 4.21, 3.55 and 3.16 eV for the above-mentioned compounds respectively.

Besides, under applied pressure, the energy band gap E_g increases to reach a maximum value about 4.34 eV (at 15 GPa), 3.91 eV (at 12 GPa) and 3.29 eV (at 2 GPa) for K_3ClO, K_3BrO, and K_3IO, respectively –these pressures will be noted P_{max} for each material–. This increment resulting of the decrease in the cell parameters, which increases the electron transition integral, this makes the band gap increase. After P_{max}, E_g decreases again to be 4.09, 3.52 and 2.48 eV at 20 GPa (see Fig. 12). These results may be caused by the existence of a phase change at different pressures noted P_{max} for each material.

TABLE 5

Calculated energy band gap (E_g) using GGA and GGA-mBJ at different pressures of K_3XO (X = Cl, B and I) compounds compared with other theoretical results

	Functional	P [GPa]	E_g [eV]		
			K_3ClO	K_3BrO	K_3IO
Other work	TB-mBJ [37]	0	—	0.93	—
	TB-mBJ [35]	0	1.00	3.65	1.11
This Work	GGA-WC	0	1.11	0.98	1.13
	TB-mBJ	0	**4.21**	**3.55**	3.16
		2	4.25	3.65	**3.29**
		4	4.27	3.71	3.16
		10	4.32	3.86	2.86
		12	3.33	**3.91**	2.75
		15	**4.34**	3.77	2.64
		20	4.09	3.52	2.48

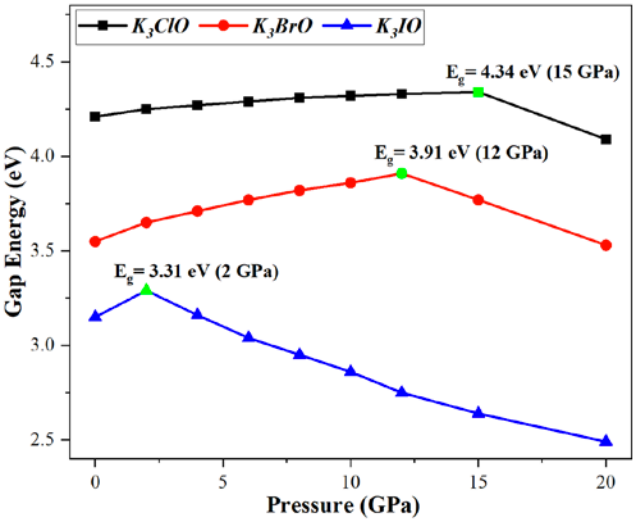

Fig. 12. Calculated energy band gap versus pressure for K_3ClO, K_3BrO, and K_3IO

3.2.2. Density Of states DOS

In order to provide more information on the different interactions between atoms and to understand the nature of the bonds present, we have calculated the total and partial density of states (DOS and PDOS) at different pressures (0 GPa and P_{max}) for each materials using GGA-WC approximation including TB-mBJ approach. The calculated DOS and PDOS of our compounds in the energy range between –6 and 7 eV are represented in Figs. 13, 14 and 15. The main observation is the presence of a forbidden zone close to the Fermi level (E_F : taken as energy reference), which confirms the semiconductor/insulator character of our materials as expected in literature [35,37]. This forbidden zone increases when going from pressure 0 to P_{max} for each compound following the shift of conduction band states to higher energies, as was observed in the band structures. In addition, in the context of our materials, it can be seen that the oxygen states (mainly *p* states) are located near the Fermi level (–1 to 0 eV) with direct and exclusive interaction with the *p* states of potassium, which explains the formation of covalent K-O bonds in all materials with a good ionic contribution due to large electronegativity difference in atoms. Moreover, a minor part of *p* states of K atoms

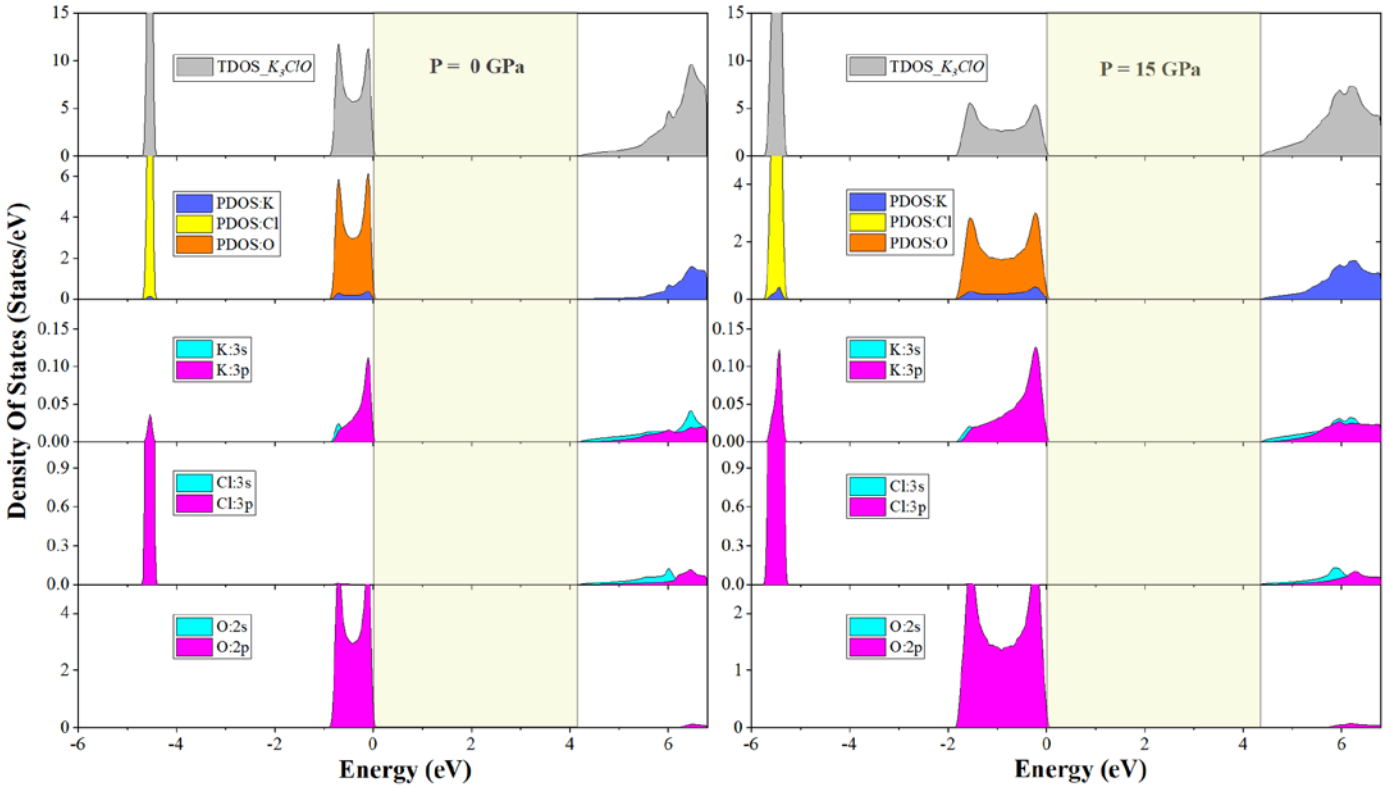

Fig. 13. Calculated TDOS and PDOS of K_3ClO at 0 and 15 GPa

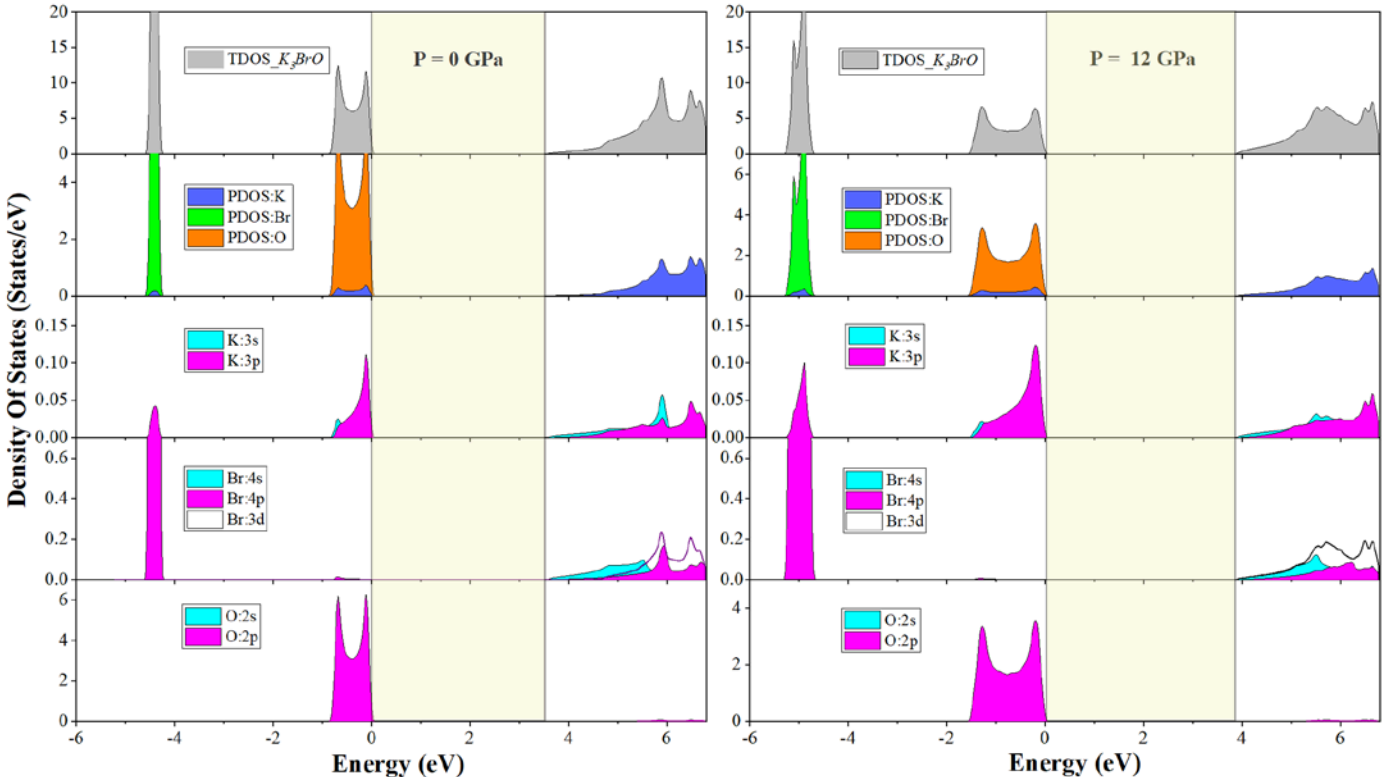

Fig. 14. Calculated TDOS and PDOS of K_3BrO at 0 and 12 GPa

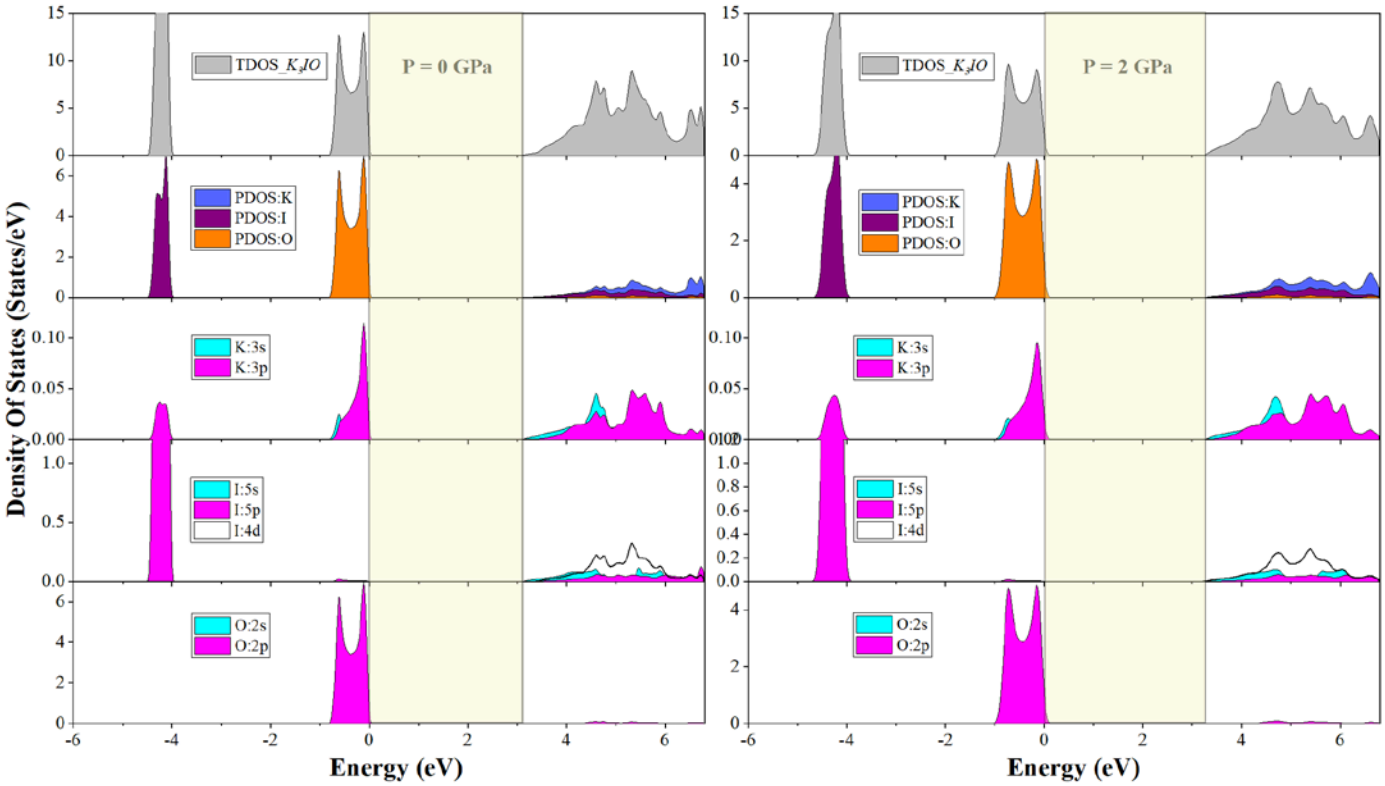

Fig. 15. Calculated TDOS and PDOS of K_3IO at 0 and 2 GPa

are in good interaction with the *p* states of halogens atoms Cl, Br and I in the region (–4 to –5 eV), resulting in a covalent character of the K-X bonds. While a significant part of *p* states of potassium are in interaction with the *d* states of halogens (Br and I) in the conduction band, resulting a double covalent-ionic character of the K-Br and K-I bonds. Hence, the ionic character of the bonding K-X gradually increases from the compound K_3ClO to K_3BrO and, ultimately, K_3IO.

3.2.3. Electronic charge densities

The electronic structure can be further analysed by examining the electronic charge distribution. Materials charge density is helpful tools for investigating their chemical bonds. The obtained results of charge density traces along the (110) plane containing the three atoms K, O and X (X = Cl, Br or I) for each compound, are illustrated in Fig. 16. A charge sharing is clearly observed between the K atom and the halogen atoms (Cl, Br or I), as well as between the K atom and the O atom. Moreover, a quasi-spherical symmetry of the charge density is particularly observed around the halogen atoms (Cl, Br or I). This indicates that the K-X bond (X = Cl, Br or I) is mainly ionic with a slight covalent tendency. Whereas the charge sharing between the K and O atoms shows the dual covalent-ionic character of the K-O bond.

3.4. Optical Properties under various pressures

The optical property is one of the most important properties of a material that may be effectively employed in both scientific investigations and the development of various devices. It is the study of the response of a material when it is irradiated by photonic energy, as it can be depended on the frequency of light. The dielectric function $\varepsilon(\omega)$ serves as a key tool for evaluating these characteristics and related parameters. The complex dielectric function is mathematically represented as the sum of two components:

$$\varepsilon(\omega)=\varepsilon_1(\omega)+i\varepsilon_2(\omega) \tag{17}$$

Where, $\varepsilon_1(\omega)$ and $\varepsilon_2(\omega)$ denote the real and imaginary part of the dielectric functions, respectively. The well-known Kramers-Kronig relations, are pivotal to determine $\varepsilon_1(\omega)$ and $\varepsilon_2(\omega)$ [59,60]:

$$\varepsilon_1(\omega)=1+\frac{2}{\pi}P\int_0^{\infty}\frac{\omega'\varepsilon_2(\omega')}{\omega'^2-\omega^2}d\omega' \tag{18}$$

$$\varepsilon_2(\omega)=\frac{2e^2\pi}{\Omega\varepsilon_0}\sum_{k,v,c}\left|\Psi_k^c\left|\hat{u}\cdot r\right|\Psi_k^v\right|^2\delta\left(E_k^c-E_k^v-E\right) \tag{19}$$

In these equations, P indicates the Cauchy principal value, a method to assign a value to an improper integral; k, v, and c denote the reciprocal lattice vector, the valence band, and the conduction band, respectively. While, the symbols u, ω, e, Ψ_k^c, and Ψ_k^v represent the incident electric field polarization vector, light frequency, electronic charge, and the wave functions of the conduction and valence bands at k, respectively. Whereas, E_k^c and E_k^v are the intrinsic energy levels. All the other optical constants can be derived from $\varepsilon_1(\omega)$ a and $\varepsilon_2(\omega)$, such absorption coefficient $\alpha(\omega)$, energy loss function $L(\omega)$, reflectivity $R(\omega)$, and Refractive index $n(\omega)$ [61]:

$$\alpha(\omega)=\sqrt{2\omega}\left(\sqrt{\varepsilon_1^2(\omega)+\varepsilon_2^2(\omega)}-\varepsilon_1(\omega)\right)^{\frac{1}{2}} \tag{20}$$

$$L(\omega)=\frac{\varepsilon_2(\omega)}{\varepsilon_1^2(\omega)+\varepsilon_2^2(\omega)} \tag{21}$$

$$R(\omega)=\left|\frac{\sqrt{\varepsilon_1(\omega)+i\varepsilon_2(\omega)}-1}{\sqrt{\varepsilon_1(\omega)+i\varepsilon_2(\omega)}+1}\right|^2 \tag{22}$$

$$n(\omega)=\frac{1}{\sqrt{2}}\left(\sqrt{\varepsilon_1^2(\omega)+\varepsilon_2^2(\omega)}+\varepsilon_1(\omega)\right)^{\frac{1}{2}} \tag{23}$$

The optical characteristics of K_3XO (X = Cl, Br, I) antiperovskite compounds have been studied in the energy range 0 eV to 25 eV and under different pressures (form 0 to 20 GPa), using TB-mBJ exchange-correlation functional due to its established level of accuracy and reliability.

The frequency dependent real part of the dielectric function $\varepsilon_1(\omega)$ is shown in Figs. 17a, 18a and 19a for K_3ClO, K_3BrO and K_3IO, respectively. When $\varepsilon_1(\omega)$ is greater than zero, the material exhibits dielectric behaviour [59], which is observed of all our compounds under study. The static dielectric constant $\varepsilon_1(0)$ increase with the increase in atomic number of X element from Cl to Br to I, and was determined to be approximately 2.05 (2.41, 2.41) for K_3ClO, 2.21 (2.51, 2.51) for K_3BrO, and 2.53 (2.63, 2.53) for K_3IO at 0 GPa (P_{max} and 20 GPa). Whereas all antiperovskite compounds exhibit maximum peaks of $\varepsilon_1(\omega)$ in the

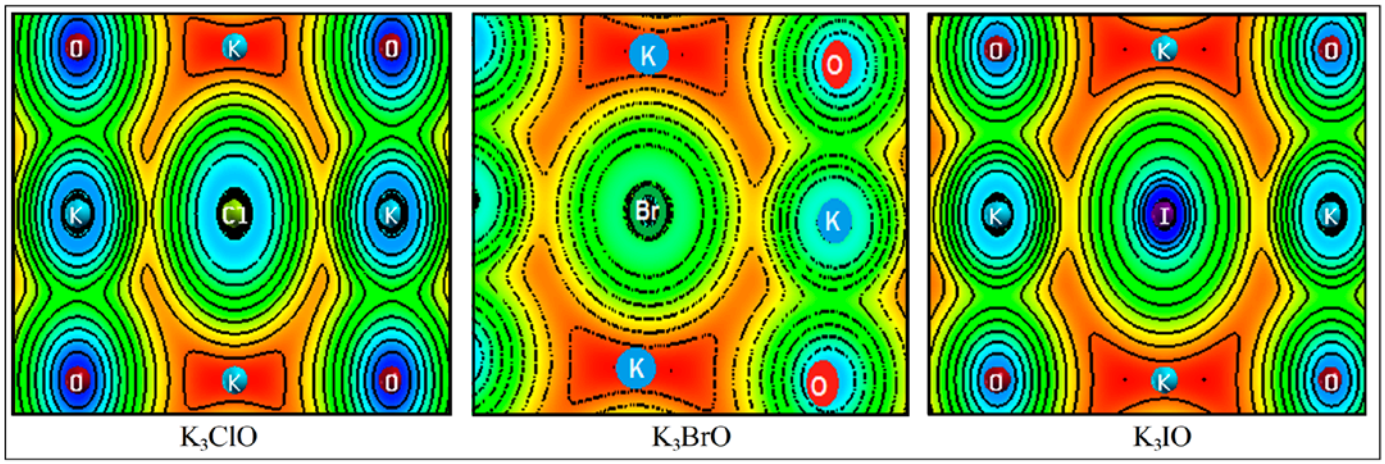

Fig. 16. Electronic charge density distribution of K_3XO (X = Cl, Br and I) at 0 GPa

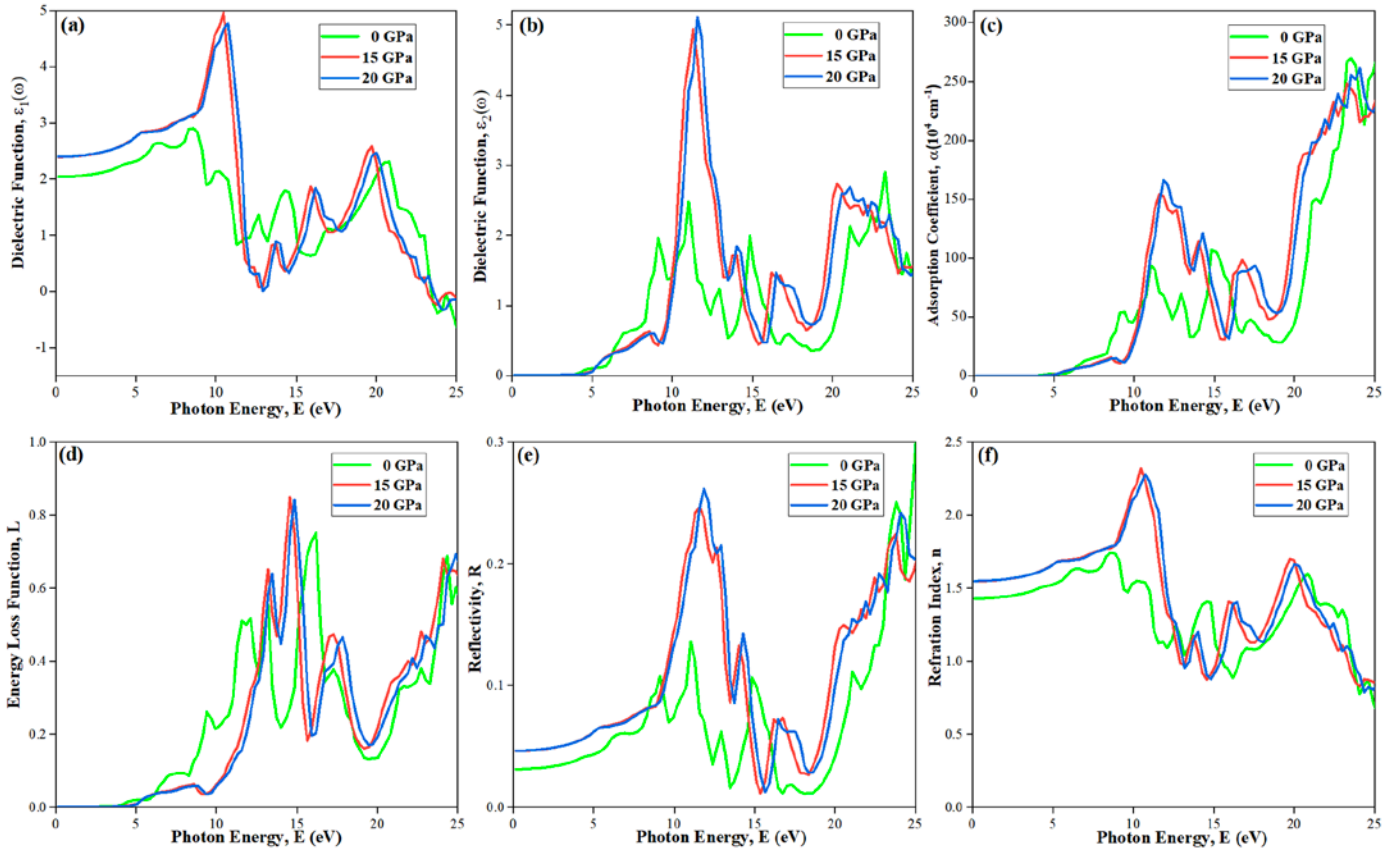

Fig. 17. a) Real part and (b) Imaginary part of dielectric function, (c) Absorption coefficient, (d) Electron energy loss, (e) Reflectivity, and (f) Refractive index of K_3ClO against pressure

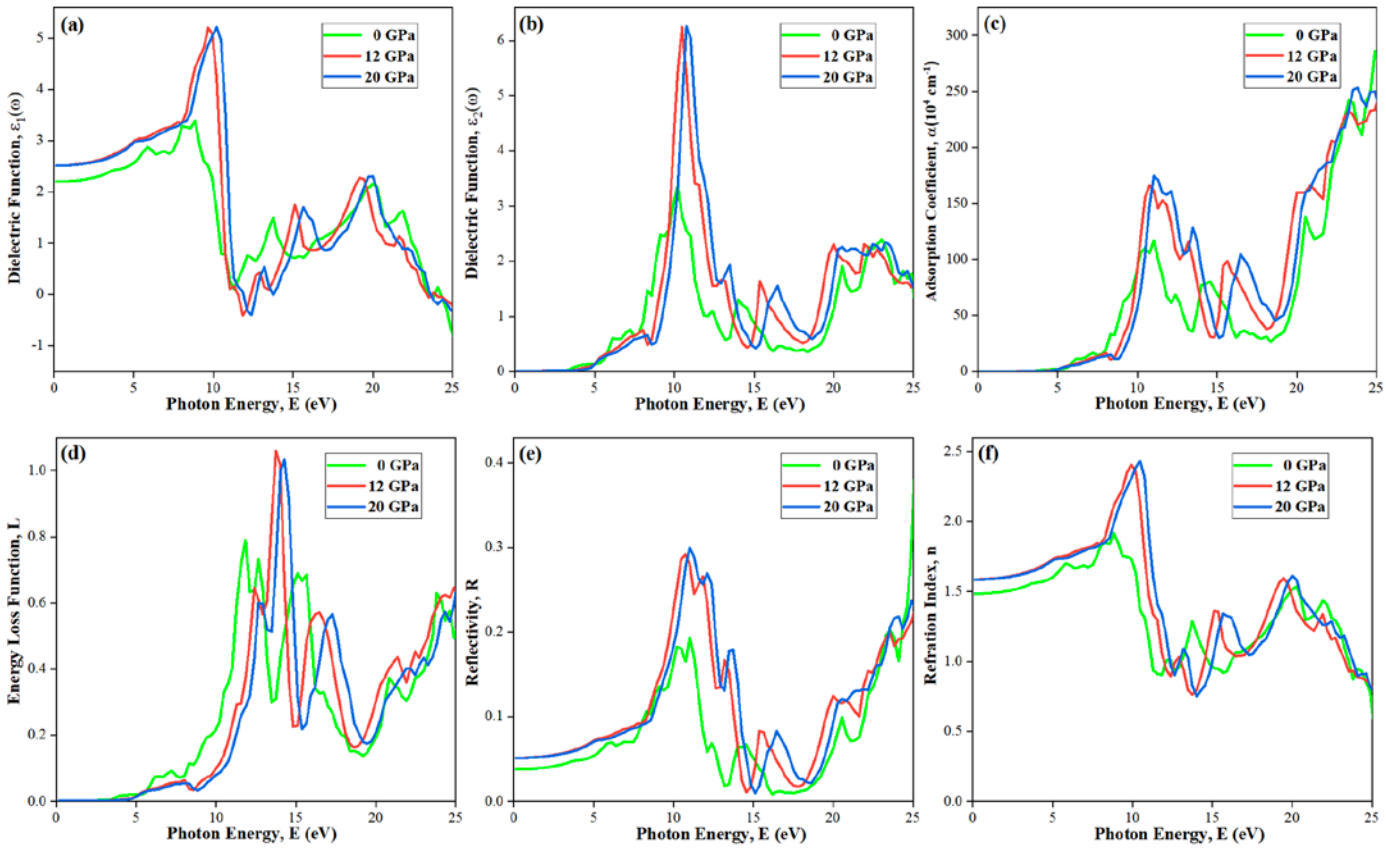

Fig. 18. a) Real part and (b) Imaginary part of dielectric function, (c) Absorption coefficient, (d) Electron energy loss, (e) Reflectivity, and (f) Refractive index of K_3BrO against pressure

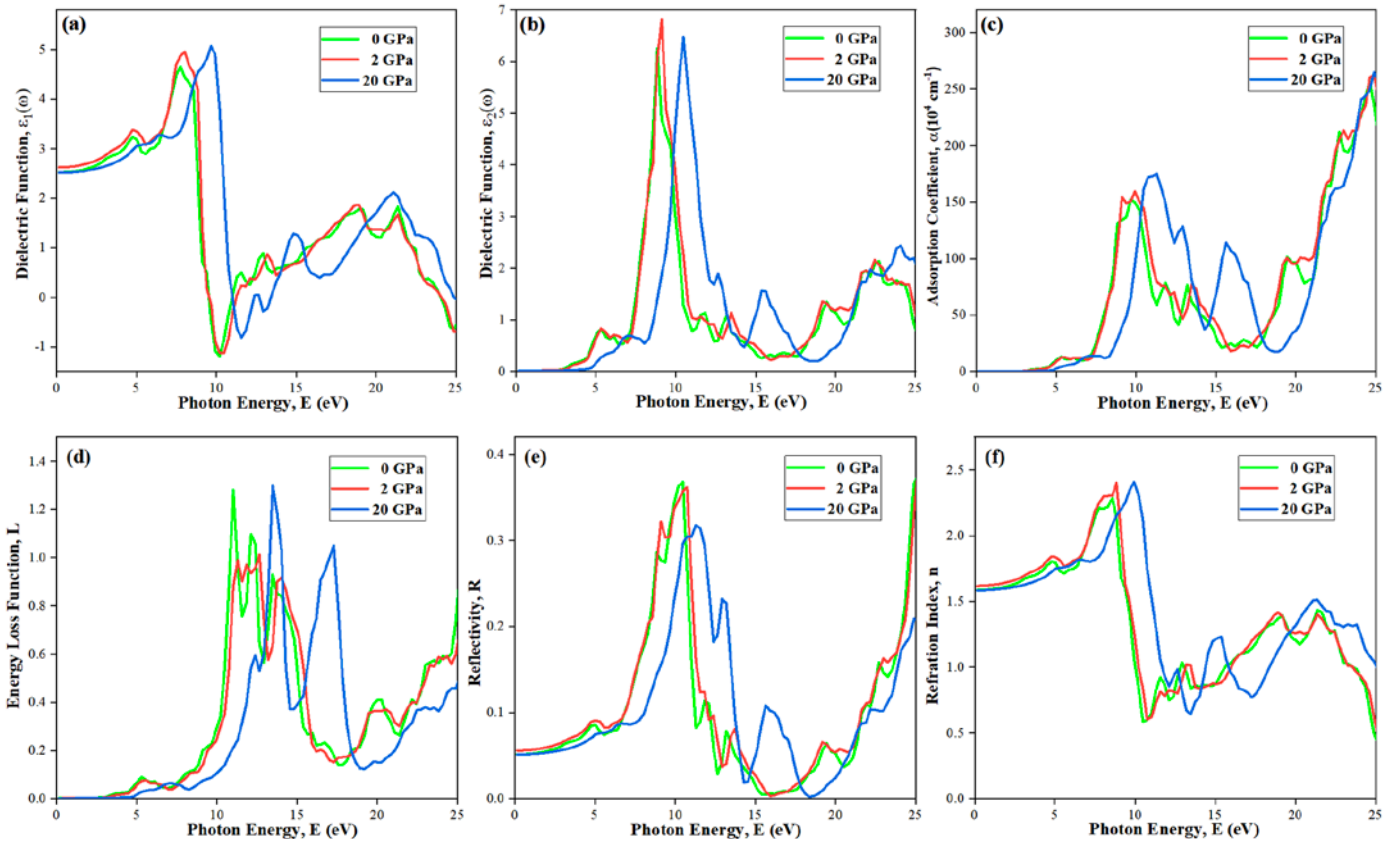

Fig. 19. a) Real part and (b) Imaginary part of dielectric function, (c) Absorption coefficient, (d) Electron energy loss, (e) Reflectivity, and (f) Refractive index of K3IO against pressure

ultraviolet (UV) spectra, about 2.92 at 8.46 eV, 3.40 at 8.85 eV and 4.64 at 7.77 eV for K_3ClO, K_3BrO and K_3IO, respectively. Moreover, this maximum of $\varepsilon_1(\omega)$ increase *vs* applied pressure to be 5 (at 15 GPa), 5.2 (at 12 GPa) and 5.1 (at 20 GPa) for K_3ClO, K_3BrO and K_3IO, respectively. It is important to mention that the excitonic peaks in the imaginary part of the dielectric function determine the interband electronic transitions due to the absorption characteristics which depends on the band structure of the material [62]. In the imaginary part $\varepsilon_2(\omega)$ represented in Figs. 17b, 18b and 19b, about six essential peaks are present, suggesting several interband transitions for our compounds which confirms their semiconductor behaviour. The observed initial excitonic peaks are 1.97 at 9.12 eV, 0.78 at 7.23 eV, and 0.82 at 5.18 eV, whereas, their maximum are 2.92 at 23.34 eV, 3.38 at 10.16 eV, and 6.26 at 8.82 eV for K_3ClO, K_3BrO and K_3IO, respectively. We note here that the maximum exciton peak increases with an increase in pressure, which means that the band is increasingly condensed, which is obvious in the calculated band structure at high pressure represented in Figs. 9, 10 and 11.

The absorption coefficient $\alpha(\omega)$ is a crucial indicator for determining the photoexcitation capabilities of materials in different energy ranges. According to the spectra shown in Figs. 17c, 18c and 19c, the absorption edges are located at about 4.2, 3.6 and 3.2 eV for K_3ClO, K_3BrO and K_3IO, respectively, which is close to the calculated energy band gap summarised in TABLE 4. Where the maximum $\alpha_{max}(\omega)$ is observed at 25, 24.8 and 24.5 eV for K_3ClO, K_3BrO and K_3IO, respectively. Furthermore, under applied pressure, the $\alpha(\omega)$ energies shift to higher values, increasing the E_g values of our oxides, as highlighted previously in the study of electronic properties. The electron energy loss function $L(\omega)$ represented in Figs. 17d, 18d and 19d, is a significant factor related to the energy loss of electrons traversing the material at high speeds and usually peaks at plasma energy or plasma frequencies [62]. The analysis of these figures allows that the plasma frequencies are about 16.1, 11.8, and 10.9 eV for K_3ClO, K_3BrO and K_3IO, respectively. These plasma frequency values are more significant under applied pressure. Figs. 17e, 18e and 19e, display the reflectivity of our materials, they show that the static reflectivity values $R_0(\omega)$ are about 3.2, 10.3, and 12.1 % for K_3ClO, K_3BrO and K_3IO, respectively. We note that the reflectivity increase with the increase in the atomic number of X element, and increase under applied pressure. In addition, the refractive index $n(\omega)$ of an optical material is crucial for its application in optical devices, it is illustrated in Fig. 17f, 18f and 19f. At zero photon energy $n_0(\omega)$, the refractive index is about 1.42 for K_3ClO, 1.48 for K_3BrO and 1.59 for K_3IO. As it is found for the reflectivity, the values of the static refractive index increase with the increase in the atomic number of X element and increase under applied pressure.

4. Conclusion

In summary, the density functional theory and FP-LAPW method have been used for studying the structural, mechanical,

electronic, and optical properties of antiperovskite compounds K_3XO (X = Cl, Br and I). The calculated lattice constants are in significant agreement with the available experimental and theoretical data. Moreover, the lattice constant increases while the bulk modulus decreases with increasing the atomic number of X element.

The calculated elastic constants obey the mechanical stability conditions reflecting the mechanical stability of all our compounds. However, the elastic constants and bulk modulus decrease while the shear modulus and Young's modulus increase with increasing the atomic number of X element. Besides, all these quantities increase with a linear dependence under an applied pressure. All three considered compounds are semiconductor with direct band gap of 4.21, 3.55 and 3.16 eV, for K_3ClO, K_3BrO and K_3IO, respectively. These values of band gap increase and decrease under applied pressure.

For the optical properties, the imaginary part of the dielectric function and the absorption coefficient of the three compounds demonstrate their suitability for optoelectronic applications, with significant absorption observed primarily in the ultraviolet (UV) range. In addition, the reflectivity of all compounds is low and not exceed 30% at 25 eV, which makes them good candidates for applications requiring very low reflectivity. Under hydrostatic pressure, most optical characteristics such as absorption coefficient, reflectivity, and refractive index of all compounds increase as the pressure increases. Our results can be considered as reliable predictions of the pressure dependence of the elastic, electronic, and optical properties of K_3ClO, K_3BrO and K_3IO compounds.

Acknowledgements

The authors wish to thank the Laboratory of Physico-chemistry of materials, Laghouat University, Algeria, for providing adequate working conditions to accomplish this work.

REFERENCES

[1] M.A. Peña, J.L. G. Fierro, Chemical Reviews **101** (7), 1981-2017 (2001).

[2] L.S. Cavalcante, V.S. Marques, J.C. Sczancoski, Chemical Engineering Journal **143**, 299-307 (2008).

[3] I. Chadli, M. Omari, M. Abu Dalo, B.A. Albiss, Journal of Sol-Gel Science and Technology **80**, 598-605 (2016).

[4] A. Chadli, B. Lagoun, L. Aissani, S. Khenchoul, I. Chadli, R. Makhloufi, E.K. Hlil, J. Electron. Mater. **50** (2), 657-663 (2021).

[5] A.S. Erchidi Elyacoubi, R. Masrour, A. Jabar, Solid State Communications **271**, 39-43 (2018).

[6] M. Jędrusik, I. Cieniek, A. Kopia, C. Turquat, C. Leroux, Arch. Metall. Mater. **65** (2), 793-797 (2020).

[7] A. Fakharuddin, U. Shabbir, W. Qiu, T. Iqbal, M. Sultan, P. Heremans, L. Schmidt-Mende, Advanced Materials **31** (47), 1807095 (2019).

[8] A.U. Abuova, Y.A. Mastrikov, E.A. Kotomin, E.A. Kotomin, S.N. Piskunov, T.M. Inerbaev, A.T. Akilbekov, J. Electron. Mater. **49**, 1421 (2020).

[9] Y. Zhang, X. Xu, AIP Adv. **10**, 035220 (2020).

[10] E. Rocha-Rangel, W.J. Pech-Rodríguez, J. López-Hernández, C.A. Calles-Arriaga, E.N. Armendáriz-Mireles, J.A. Castillo-Robles, J. a. Rodríguez-García, Arch. Metall. Mater. **65** (2), 621-626 (2020).

[11] R. Masrour, A. Jabar, A. Benyoussef, M. Hamedoun, E.K. Hlil, Journal of Magnetism and Magnetic Materials **401**, 91-95 (2016).

[12] H. Han, S. Song, J.H. Lee, K.J. Kim, G.-W. Kim, T. Park, H.M. Jang, Chem. Mater. **27**, 7425 (2015).

[13] A.M. Elseman, F.A. Ali, E. Ewais, I. Ibrahim, M.M. Rashad, Critical Reviews in Solid State and Materials Sciences, 1-29 (2025).

[14] W. Xia, Y. Zhao, F. Zhao, K. Adair, R. Zhao, S. Li, et al., Chemical Reviews **122** (3), 3763-3819 (2022).

[15] Z.-L. Lv, Physica Status Solidi B, **254**, 1700089 (2017).

[16] M. Bilal, S.M. Alay-e-Abbas, M. Sluydts, J. Batool, A. Laref, G. Abbas, N. Amin, Physics Letters A **408**, 127469 (2021).

[17] N. Hoffmann, T.F.T. Cerqueira, J. Schmidt, M.A.L. Marques, npj Computational Materials **8**, 150 (2022).

[18] X.H. Zhang, Y. Yin, Q. Yuan, J.C. Han, Z.H. Zhang, J.K. Jian, J.G. Zhao, B. Song, Journal of Applied Physics **115**, 123905 (2014).

[19] T. Shibayama, K. Takenaka, Journal of Applied Physics **109**, 07A928 (2011).

[20] L. Zu, S. Lin, J. Lin, B. Yuan, X. Kan, P. Tong, W. Song, Y. Sun, Inorganic Chemistry **55**, 9346-9351 (2016).

[21] H.K. Singh, Z. Zhang, I. Opahle, D. Ohmer, Y. Yao, H. Zhang, Chemistry of Materials **30** (20), 6983 (2018).

[22] Y. Wang, Q. Wang, Z. Liu, Z. Zhou, S. Li, J. Zhu, R. Zou, Y. Wang, J. Lin, Y. Zhao, Journal of Power Sources **293**, 735 (2015).

[23] S. Uddin, A. Das, M.A. Rayhan, S. Ahmad, R.M. Khokan, M. Rasheduzzaman, M.Z. Hasan, Journal of Computational Electronics **23**, 1217-1237 (2024).

[24] Z. Deng, D. Ni, D. Chen, Y. Bian, S. Li, Z. Wang, Y. Zhao, InfoMat. **4** (2), e12252 (2022).

[25] Y. Zhao, L.L. Daemen, Journal of the American Chemical Society **134** (36), 15042-15047 (2012).

[26] Y. Zhao, C. Lian, S. Zeng, Z. Dai, S. Meng, J. Ni, Physical Review B **102** (9), 094314 (2020).

[27] S. Zeng, L. Guo, Z. Huang, Q. Shen, Y. Zhao, H. Huang, Y. Tu, Chemistry of Materials **36** (1), 211-218 (2023).

[28] Y. Sun, X.Q. Chen, S. Yunoki, D. Li, Y. Li, Physical Review Letters **105** (21), 216406 (2010).

[29] T.H. Hsieh, J. Liu, L. Fu, Physical Review B **90** (8), 081112 (2014).

[30] H. Sabrowsky, K. Paszkowski, D. Reddig, P. Vogt, Zeitschrift für Naturforschung B **43** (2), 238-239 (1988).

[31] K. Hippler, S. Sitta, P. Vogt, H. Sabrowsky, Crystal Structure Communications **46** (5), 736-738 (1990).

[32] S. Sitta, K. Hippler, P. Vogt, H. Sabrowsky, Zeitschrift für Anorganische und Allgemeine Chemie **597** (1), 197-200 (1991).

[33] S. Sitta, K. Hippler, P. Vogt, H. Sabrowsky, Zeitschrift für Kristallographie **196** (1-4), 193-196 (1991).

[34] V.I. Zinenko, N.G. Zamkova, Ferroelectrics **265** (1), 23-29 (2002).

[35] J. Ramanna, N. Yedukondalu, K.R. Babu, G. Vaitheeswaran, Solid State Sciences **20**, 120-126 (2013).
[36] S.A. Khandy, I. Islam, A. Laref, M. Gogolin, A.K. Hafiz, A.M. Siddiqui, International Journal of Energy Research **44**, 2594-2603 (2020).
[37] M.A. Sattar, M. Javed, M. Benkraouda, N. Amrane, International Journal of Energy Research **45** (3), 4793-4810 (2021).
[38] P. Hohenberg, W. Kohn, Physical Review **136**, B864 (1964).
[39] W. Kohn, L.J. Sham, Physical Review **140**, A1133 (1965).
[40] P. Blaha, K. Schwarz, P. Sorantin, S. Trickey, Computer Physics Communications **59** (2), 399-415 (1990).
[41] P. Blaha, K. Schwarz, F. Tran, R. Laskowski, G.K. Madsen, L.D. Marks, Journal of Chemical Physics **152** (7), 074101 (2020).
[42] Z. Wu, R.E. Cohen, Physical Review B **73**, 235116 (2006).
[43] F. Tran, P. Blaha, Physical Review Letters **102**, 226401 (2009).
[44] H.J. Monkhorst, J.D. Pack, Physical Review B **13** (12), 5188 (1976).
[45] F. Birch, Physical Review **71**, 809 (1947).
[46] S.A. Muslov, A.I. Lotkov, S.D. Arutyunov, Russian Physics Journal **62**, 1417-1427 (2019).
[47] M.J. Mehl, B.M. Klein, D.A. Papaconstantopoulos, Intermetallic Compounds: Principles and Practice **1**, 195-210 (1994) .
[48] P. Ravindran, L. Fast, P.A. Korzhavyi, B. Johansson, Journal of Applied Physics **84** (9), 4891 (1998).
[49] W. Voigt, Lehrbuch der Kristallphysik, Teubner-Verlag, Leipzig (1928).
[50] A. Reuss, Journal of Applied Mathematics and Mechanics **9**, 49 (1929).
[51] R. Hill, Proceedings of the Physical Society A **65**, 349 (1952).
[52] A. Yildirim, H. Koc, E. Deligoz, Chinese Physics B **21** (3), 037101 (2012).
[53] S. Ayhan, G. Kavak, Materials Research Express **6**, 0865e9 (2019).
[54] R. Paudel, J. Zhu, Physica B **557**, 45-51 (2019).
[55] J. F. Nye, Properties of Crystals, Oxford University Press, New York (1985).
[56] E. Schreiber, O.L. Anderson, N. Soga, Elastic Constants and Measurements, McGraw-Hill, New York (1973).
[57] O. L. Anderson, Journal of Physics and Chemistry of Solids **24** (7), 909-917 (1963).
[58] W. Setyawan, S. Curtarolo, Computational Materials Science **49**, 299 (2010).
[59] R. Charif, R. Makhloufi, S.C. Mouna, A. Chadli, A. Barkat, M. Nouiri, Physica Scripta **99** (12), 125909 (2024).
[60] G. Essalah, G. Kadim, A. Jabar, R. Masrour, M. Ellouze, H. Guermazi, S. Guermazi, Ceramics International **46** (8), 12656-12664 (2020).
[61] H. Rached, D. Rached, M. Caid, L. Amrani, Y. Rached, H. Mansour, N.T. Mahmoud, S. Al-Qaisi, M. Alyami, A.A. Ait Belkacem, J. Inorg. Organomet. Polym. **35**, (2025).
[62] A.A. Sholagberu, W.A. Yahya, A.A. Adewale, Physica Scripta **97** (8), 085824 (2022).